ACS APPLIED NANO MATERIALS

www.acsanm.org
Article

Confining the Synthesis of Palladium Nanoparticles in Mesoporous Silicas for CO Oxidation: The Role of the Support

Francesca Tajoli, Paolo Dolcet, Sarah Claas, Carina B. Maliakkal, Di Wang, Christian Kübel, Maria Casapu, Michael Fröba, Jan-Dierk Grunwaldt, and Silvia Gross*

Cite This: https://doi.org/10.1021/acsanm.4c05689

ABSTRACT: The synthesis of palladium (Pd) nanoparticles (NPs) in the highly constrained pore network of mesoporous silicas is systematically investigated for the first time, comparing the synthesis outcomes with a reference sample of Pd NPs on the outer surface of nonporous silica. Two different families of mesoporous silica (SBA-15 and KIT-6), with different pore arrangements and connectivity, as well as two different pore sizes within both porous systems (i.e., 7 and 9 nm), are investigated as supports for Pd NPs synthesis, and the effect of mesopore confinement is explored. In particular, the mesoporous matrixes allow one to obtain smaller and homogeneously distributed Pd NPs with respect to the nonporous support, and their actual location within the mesopore-constrained environment is confirmed by electron tomography. Moreover, the application of Pd NPs on mesoporous and nonporous silicas as heterogeneous catalysts for CO oxidation is explored, and the noticeable stability of Pd NPs on the supports is assessed by probing the accessibility and dynamic response of Pd species by *operando* Pd K-edge X-ray absorption spectroscopy measurements. Oxidized Pd species are found to be the active phase of the catalytic reaction, and the complex interplay of several factors occurring in regulating the catalytic activity of the supported NPs is discussed.

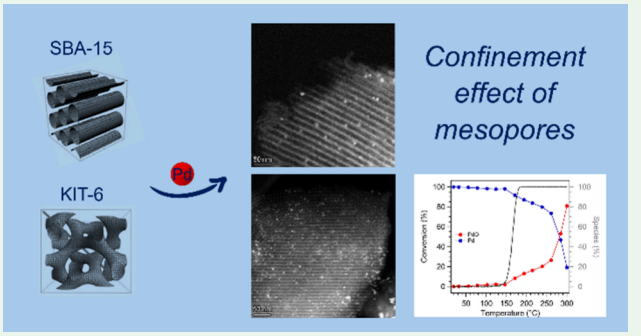

KEYWORDS: *palladium, mesoporous silica, space confinement, heterogeneous catalysis, CO oxidation, operando XAS*

INTRODUCTION

Thanks to their regular pore arrangement and narrow pore-size distribution, mesoporous materials (pore diameter 2−50 nm)[1] with ordered structure are of great interest for size- and shape-selective applications, such as molecular sieves[2] and catalysis[3,4] or as host structures for nanometer-sized guest compounds.[5] Indeed, their uniform mesoporous structure provides a size-selective nanoenvironment that can be exploited, for example, for supporting metal nanoparticles (NPs) with a homogeneous distribution.

Among mesoporous materials, silica is one of the most widely studied because highly ordered mesopore architectures, with tunable pore size, arrangement, and accessibility, can be readily synthesized by using soft templating methods. Thanks to their high specific surface area (SSA; 700−900 $m^2 \cdot g^{-1}$) and large porosity, combined with a high-quality structure regularity, mesoporous silica materials are widely used as supports in the field of catalysis.[6] Indeed, the very ordered, uniform, and controllable pore structure of mesoporous silica plays an important role in NPs distribution within the support, which is desired to be homogeneous to limit aggregation phenomena and particle sintering at elevated temperatures, under catalytic operating conditions.

In this context, supported platinum-group metal NPs are widely exploited in several fields of catalysis and energy-related processes such as, e.g., environmental and hydrogenation catalysis as well as electrocatalysts. Indeed, it is well-known that the size of noble-metal NPs plays a crucial role in ruling their catalytic activity, selectivity, and stability, as well as that a major relevance is also held by the nature, structure, and morphology of the support, which can be active (e.g., ceria: as a reducible oxide, it can act as oxygen storage for oxidation reactions)[7] or inert (e.g., alumina or silica).[8,9] Among inert supports, high-SSA silica has emerged as an attractive environment for supporting metallic NPs thanks to its low cost, easy preparation, high chemical and thermal stability, and tunable porosity.

Within this framework, the synthesis of palladium (Pd) NPs inside the pores of mesoporous silica materials by the incipient wetness impregnation (IWI) technique was addressed to

Received: October 7, 2024
Revised: January 6, 2025
Accepted: January 20, 2025

investigate the effect of spatial confinement, offered by differently sized and interconnected mesopores with different arrangement and accessibility, on the size and size distribution of the supported NPs and on their distribution across the porous network. Indeed, confined space represents a fascinating and still relatively uncharted playground for the spatially controlled formation of inorganic NPs because it plays a crucial role in the outcome of the syntheses that are performed within it. However, interesting variations in the properties of the formed nanomaterials emerge only when the confined space has a smaller dimension. In particular, in order to unveil the effect of the arrangement and accessibility of pores, as well as their dimensions (i.e., effect of space confinement) on the Pd NPs, two different families of mesoporous silica (i.e., SBA-15 and KIT-6) and two different pore sizes in the lower nanometer range (i.e., 7 and 9 nm) within both families of materials were addressed. Moreover, to comprehensively study the effect of spatial confinement provided by the mesopores on the final size and crystal structure of Pd NPs, a silica commercial reference with a lower SSA (Aerosil 200, Degussa GmbH) was also investigated as a reference support (no space confinement and equivalent heterogeneous nucleation over the surface of silicon oxide). To the best of our knowledge, no systematic study based on the controlled variation of the structural and morphological features of the support, specifically in terms of the pore size and connectivity, has been undertaken yet. Indeed, a thorough comparison of the effect of both spatial confinement (i.e., porous vs nonporous support) and constraint parameters (e.g., confined space size and connectivity) has not been addressed by the very few reports in the literature on Pd NPs synthesis inside a mesoporous silica network.[10−13] A first comparative study has been reported by Parlett et al.,[14] who, however, focused their work on investigating the role of mesopore interconnectivity on the activity in the aerobic oxidation of allylic alcohols and not on the Pd NPs synthesis outcome (i.e., crystallization in confined space).

Finally, the mesoporous and nonporous silica-supported Pd NPs were tested as heterogeneous catalysts for CO conversion (Figure 1). This process was chosen as a model reaction for the

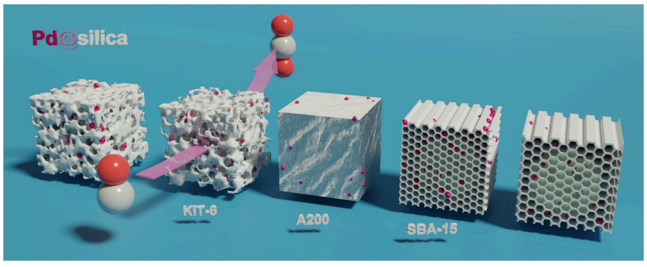

Figure 1. Schematic representation of the investigated Pd NPs (pink) supported on mesoporous (SBA-15 and KIT-6) and nonporous (A200) silica materials (white), highlighting their application as heterogeneous catalysts for CO oxidation.

catalytic oxidative reactions to probe the redox response and accessibility of Pd species, as well as the material stability. The changes in the Pd oxidation state were correlated with their catalytic activity during *operando* X-ray absorption spectroscopy (XAS) experiments, providing for the first time fundamental insight on the functionality of mesoporous silica-supported Pd NPs as heterogeneous catalysts.

EXPERIMENTAL SECTION

Chemicals. Pluronic P-123 [poly(ethylene glycol)-*block*-poly(propylene glycol)-*block*-poly(ethylene glycol)] was purchased from Sigma-Aldrich. Tetraethyl orthosilicate (TEOS, for synthesis) and hydrochloric acid (32 wt %, for analysis, EMSURE) were obtained from Merck. 1-Butanol (≥99.5%, for synthesis) was purchased from Carl Roth. Palladium nitrate hydrate was purchased from Merck. Aerosil 200 was purchased from Degussa GmbH. Hydrogen, helium, carbon monoxide (5 vol % He), and oxygen (10 vol % He) were purchased from Alphagaz. All chemicals were of analytical grade and were used as received without any further purification.

Synthesis of Mesoporous Silica Materials. The synthesis of the mesoporous silica material SBA-15 was performed according to the instructions of Speil et al.[15] Pluronic P-123, water, and HCl (32 wt %, 1.16 mol) were mixed, heated to 35 °C, and stirred for 15.5 h in a closed screw-cap flask. Subsequently, TEOS (116 mmol) was added, and the resulting mixture was stirred for another 24 h at 35 °C. Afterward, the reaction solution was solvothermally treated under static conditions for 24 h at different temperatures to control the final mesopore size (80 and 120 °C for the *A* and *C* series, respectively). Next, the reaction mixture was filtered and washed with water (1 L) and ethanol (200 mL). The product was dried at 60 °C, and the structure-directing agent was removed by calcination in static air at 550 °C for 5 h with a heating rate of 1 °C·min^{-1}.

The synthesis of the mesoporous silica materials KIT-6 was carried out according to a slightly modified procedure based on that used by Kleitz et al.[16] Pluronic P-123, water, and HCl (32 wt %, 1.16 mol) were mixed, heated to 35 °C, and stirred for 15.5 h in a closed screw-cap flask. Subsequently, 1-butanol (162 mmol) and TEOS (116 mmol) were added, and the resulting mixture was stirred for another 24 h at 35 °C. Afterward, the reaction solution was solvothermally treated under static conditions for 24 h at different temperatures to control the final mesopore size (80 and 120 °C for the *A* and *C* series, respectively). Next, the reaction mixture was filtered and washed with water (1 L) and ethanol (200 mL). The product was dried at 60 °C, and the structure-directing agent was removed by calcination in static air at 550 °C for 5 h with a heating rate of 1 °C·min^{-1}.

The exact amounts used and the synthesis conditions are shown in Table S1. Table S2 displays mesoporous and nonporous silica samples. The as-prepared mesoporous silica materials are referred to as the *pristine* series (*prist* in the sample names).

Synthesis of Pd NPs Supported on Mesoporous and Nonporous Silicas. Pd NPs were synthesized directly into the pores of mesoporous and nonporous silica through two subsequent cycles of IWI, followed by slow drying at 50 °C for 18 h. More specifically, a Milli-Q water solution of $Pd(NO_3)_2$ was added to the pristine silica material, using a volume equal to the total pore volume of the support to be filled (determined by N_2 physisorption measurements) and a concentration such as to obtain a final composition of 2 wt % Pd@SiO_2 after two subsequent cycles of IWI (Table 1). For the batch nonporous silica sample, the volume of the $Pd(NO_3)_2$ impregnation solution could not be determined based on the volume of pores to be filled, as for mesoporous samples. Thus, the synthesis was performed by employing a volume and concentration of a $Pd(NO_3)_2$ impregnation solution equal to those employed with the mesoporous sample with the lowest pore volume (sample KA; Table 1). The as-prepared samples are referred to as the *impregnated* series (*impr* in the sample names).

The impregnated samples were then treated at 150 °C in a reducing atmosphere (5 vol % H_2/He; total flow 100 mL·min^{-1}) for 30 min in a tubular furnace (Gero) to mildly reduce the impregnated Pd(II) precursor to Pd(0) (*reduced* series, *red* in the sample names). Because the preparation of the nanomaterials encompassed several synthetic steps (i.e., preparation of the mesoporous support, two subsequent steps of impregnation followed by thermal treatment and reduction) and was extremely time and experimentally demanding, only one replicate was performed.

Testing of the Catalytic Activity for CO Oxidation. The catalytic activity tests were carried out on an in-house-built setup,

https://doi.org/10.1021/acsanm.4c05689
ACS Appl. Nano Mater. XXXX, XXX, XXX−XXX

Table 1. Experimental Conditions Employed for the Impregnation of Mesoporous and Nonporous Silica with 2 wt % Pd

	sample name	specific V_{pores} [$cm^3 \cdot g^{-1}$]	m_{SiO_2} [g]	total V_{pores} [cm^3]	Pd loading [wt %][a]	conc $Pd(NO_3)_2$ solution [M]	$V_{Pd(NO_3)_2}$ solution [mL][b]
mesoporous silica	SA	0.985	0.980	0.965	1	0.097	0.965
	SC	1.32	0.980	1.30	1	0.073	1.30
	KA	0.905	0.980	0.887	1	0.106	0.887
	KC	1.50	0.980	1.47	1	0.064	1.47
nonporous silica	A200	-	0.980	-	1	0.106	0.887

[a]Pd loading per impregnation step. After two IWI cycles (i.e., impregnation and drying), the final Pd loading is 2 wt %. [b]Volume of $Pd(NO_3)_2$ solution added per impregnation step.

shown in Figure S1, with a geometry similar to that further used during the *in situ/operando* experiments at the synchrotron (see corresponding section below). A hot-air gas blower (Oxford), operated by in-house *LabView* software, was employed as the heating source. EL-FLOW Select (Bronkhorst) mass flow controllers (MFCs) and stainless-steel piping lines were used for gas (He, O_2, CO, and H_2) dosing into the reactor. The concentrations of CO and CO_2 in the product flow were monitored online with a Fourier transform infrared spectrometer (MultiGas 2030 FTIR continuous gas analyzer, MKS Instruments) and an Omnistar mass spectrometer (Pfeiffer Vacuum).

An exact amount of about 2.5 mg of a sieved fraction of size 125−250 μm of the samples, in a physical mixture with silica (1:1 by weight; total amount = 5.0 mg; dilution with silica is needed to avoid the formation of hot spots that might occur in the case when a small volume of pure catalyst is employed), was loaded into a quartz glass plug flow reactor (1.5 mm i.d.) and treated with three consecutive catalytic cycles (light-off and light-out) up to 300 °C (heating rate of 10 °C·min^{-1}). A gas mixture composed of 1000 ppm of CO and 9 vol % O_2 in He was applied at a total gas flow of 50 mL·min^{-1} and a weight hourly space velocity (WHSV) of 60000 L·h^{-1}·g_{Pd}^{-1}. Then, an *in situ* reduction step was performed by feeding 2.5 vol % H_2 in He into the reactor, heating it up to 150 °C (heating rate of 10 °C·min^{-1}), holding the temperature at 150 °C for 30 min, and further cooling in He. After the reduction step, three additional catalytic cycles were conducted. A schematic representation of the sequence of catalytic tests and further treatment performed is reported in Figure S2.

N_2 Physisorption. N_2 adsorption−desorption isotherms were recorded at −196 °C (77 K) using a Micromeritics ASAP 2020 Plus Instrument. Before the measurements, samples were degassed at 100 °C for 20 h under vacuum to ensure the complete removal of any previous adsorbate. The SSA of the samples was calculated by a multipoint Brunaer−Emmett−Teller (BET) analysis in the 0.04−0.18 p/p_0 range. The partial pressure ranges were selected for each sample according to the Rouquerol criteria, in order for the isothermal adsorption data to meet the assumptions of BET analysis.[17] The mesopore size distributions were estimated by the density functional theory (DFT) method [nonlocalized DFT (NLDFT) kernel for silica, −196 °C, cylindrical pores, adsorption branch] employing the *QuantaWin* software from Quantachrome Instruments. The total pore volume was determined from the amount of vapor adsorbed at p/p_0 = 0.95.

Transmission Electron Microscopy (TEM), Scanning Transmission Electron Microscopy (STEM), and Electron Tomography. TEM measurements of pristine SBA-15 and KIT-6 were recorded using a JEOL JEM 1011 with an acceleration voltage of 100 kV. Images were acquired with a SIS CCD camera system (1376 × 1032 px). The samples were dispersed with ethanol and dripped onto a TEM grid. After complete evaporation of the solvent, the samples were measured. TEM measurement of a pristine A200 support was carried out using a Tecnai G^2 (FEI) instrument, operating at 100 kV. Images were acquired with a Veleta digital camera. Samples were prepared by depositing a droplet of powder suspension in ethanol on a 400-mesh holey film Cu grid. STEM of reduced Pd@SiO_2 samples prior to and after catalysis was performed with a double-corrected Thermo Fischer Themis Z or a probe-corrected Thermo Fischer Themis 300 electron microscope, which was operated at 300 keV, at the KNMFi located at the INT at KIT. STEM images were obtained using a high-angle annular dark-field (HAADF) detector. Energy-dispersive X-ray (EDX) spectroscopy elemental maps were obtained using a Super-X detector in STEM mode. HAADF and EDX spectral imaging were acquired and processed using *Velox* software. Dimensional analysis of Pd NPs was manually performed using Fiji software (*ImageJ*, version 1.54f).[18,19] To analyze the spatial distribution of Pd NPs in three dimensions, electron tomography was utilized. A series of STEM images were taken of selected sample regions over tilts ranging approximately from +70° to −70° in 2° intervals using the Tomography STEM software. Alignment of the tilt series was done using *ETomo/Imod 4.7* software with residual errors below 1 pixel for the 1024 × 1024 pixels image series and less than 2 pixels for the 2048 × 2048 pixels image series. Reconstruction of the three-dimensional (3D) volume was done using the SIRT algorithm implemented in *Inspect3D V4,4*. 3D visualization was done in Avizo version 2021.1. More technical details are included in the metadata provided.

X-ray Absorption Spectroscopy (XAS). The Pd K-edge (24350 eV) XAS spectra, in terms of X-ray absorption near-edge structure (XANES) and extended X-ray absorption fine structure (EXAFS) of reference Pd-containing compounds (e.g., PdO, palladium nitrate, metallic Pd) and powdered samples, were collected at the SAMBA beamline of the SOLEIL synchrotron. All samples were measured *ex situ* either as pellets using cellulose as the binder or, in the case of the catalysts, as pure powder.

In situ/operando XAS measurements at the Pd K-edge (24350 eV) were conducted during the temperature-programmed reduction (TPR) and catalytic CO oxidation for selected catalyst samples, at the same beamline. A capillary microreactor was used as an *in situ/operando* cell at the beamline, analogous to the lab experiments, using a capillary oven available at the beamline as the heating source.[20] For gas dosing and related analytics, the same portable setup was also used at the beamline. Gas doses were controlled by EL-FLOW Select (Bronkhorst) MFCs, and the gas concentration in the product flow was monitored online by a Fourier transform infrared spectrometer (MultiGas 2030 FTIR continuous gas analyzer, MSK Instruments) and a mass spectrometer (Omnistar, Pfeiffer Vacuum).

The capillary reactor was loaded with 5.0 mg of the granulated (125−250 μm) sample. At first, the *in situ* reduction step (TPR) was performed, treating the impregnated samples with 2.5 vol % H_2 in He while heating up to 150 °C (heating rate of 10 °C·min^{-1}) and holding the temperature at 150 °C for 30 min. Subsequently, two consecutive catalytic cycles (light-off/light-out) were carried out between 50 and 300 °C (heating rate of 10 °C·min^{-1}) in a gas mixture composed of 1000 ppm of CO and 10 vol % O_2 in He, with a total flow of 100 mL·min^{-1} and a WHSV of 60000 L·h^{-1}·g_{Pd}^{-1}. A schematic representation of the treatment performed is shown in Figure S3.

During the above-described sample treatment, XANES spectra at the Pd K-edge (24350 eV) were collected in transmission mode in the 24150−24850 eV range. Due to the heating rate of 10 °C·min^{-1} and XANES collecting time, each spectrum corresponds to a ca. 30 °C variation step. At the beginning of the procedure and after each cycle, five EXAFS spectra were acquired at room temperature in air and/or in a reaction mixture in the 24.15−25.5 keV range. A Si(311) monochromator was employed for energy selection, and the beam spot size on the sample was ca. 0.5 mm × 1 mm. Energy calibration

https://doi.org/10.1021/acsanm.4c05689
ACS Appl. Nano Mater. XXXX, XXX, XXX−XXX

Table 2. Structural Parameters of Pristine Silica Supports Derived from N_2 Physisorption and Low-Angle XRD Measurements

	silica support	sample name	SSA_{BET} [$m^2 \cdot g^{-1}$][a]	d_{DFT} [nm][b]	V_t [$cm^3 \cdot g^{-1}$][c]	a [nm][d]	t_{wall} [nm][e]
mesoporous silica	SBA-15	*SAprist*	930	7.0	0.985	10.4	3.4
		SCprist	743	8.8	1.32	11.4	2.6
	KIT-6	*KAprist*	766	6.8	0.905	20.6	3.3
		KCprist	691	8.8	1.50	23.5	3.2
nonporous silica	Aerosil 200	*A200prist*	189				

[a]Specific surface area determined by means of the BET equation. [b]Mean mesopore diameter estimated via the DFT model. [c]Total pore volume. [d]Unit cell parameter a estimated by XRD, as $a = 2d_{(100)}/\sqrt{3}$ and $a = \sqrt{6}\,d_{(211)}$ for SBA-15 and KIT-6 silicas, respectively; [e]Silica wall thickness t_{wall} calculated from a and d_{DFT}, as $t_{wall} = a - d_{DFT}$ and $t_{wall} = (a/3.092) - d_{DFT}/2$, for SBA-15 and KIT-6 silicas, respectively.

was carried out using the position of the Pd K-edge of the spectrum of a Pd foil as a reference, measured behind the sample and second ionization chamber. The employed experimental setup is shown in Figure S4.

Data reduction and treatment were performed using the *FASTOSH* software (version 1.0.2),[21] developed at the SAMBA beamline. For the linear combination fitting (LCF) of the XANES data acquired during TPR and catalytic testing, the spectra of metallic Pd and PdO were used as references. The data range used for the LCF was 24320−24400 eV.

X-ray Photoelectron Spectroscopy (XPS). XPS spectra were collected with a ThermoScientific Escalab QXi spectrometer, using a monochromated, microfocused Al Kα source (spot size diameter = 650 μm). Survey spectra were collected in the range −5 to −1350 eV, with a pass energy of 50 eV, a step size of 1 eV, and a dwell time of 100 ms·step^{-1}. Detailed spectra of regions of interest (Si 2p, O 1s, Pd 3d, and C 1s) were collected with a pass energy of 50 eV, a step size of 0.05 eV, and a dwell time of 50 ms·step^{-1}. Charge compensation was applied to avoid the charging effects. Quantification of the species and further analysis of the spectra were carried out using ThermoScientific Avantage software (version 6.7.0).

X-ray Diffraction (XRD). Low-angle and wide-angle XRD patterns of the samples were acquired using a Bruker AXS D8 Advance Plus diffractometer, equipped with a Cu K$\alpha_{1,2}$ anode (λ = 1.5106 Å) and mounted with a LYNEXEYE XE-T detector employed in 1D mode. X-rays were generated by supplying a voltage of 40 kV and a current of 40 mA to the Cu anode, and data were collected with Bragg−Brentano geometry. Low-angle XRD data were collected over the 0.4−6.0° 2θ range, with a step size of 0.02° 2θ and a nominal time per step of 1 s. A variable primary divergence slit opening (keeping the length of the illuminated specimen area constant to 25 mm) and a fixed secondary divergence slit opening (2.34°) were employed together with Soller slits with an aperture of 2.5°. A position-sensitive detector (PSD) opening of 0.4° was employed. Automatic air scatter knife positioning was used. Wide-angle XRD patterns were acquired in the 15−90° 2θ range, with a step size of 0.02° 2θ and a nominal time per step of 0.5 s. Fixed divergence slits of 0.50° were employed together with Soller slits with an aperture of 2.5°. A maximum PSD opening was used (2.83°). Data were analyzed with the Bruker *Diffrac.Suite* (version 6.0.0.6).

RESULTS AND DISCUSSION

Pristine Mesoporous and Nonporous Silica Supports. The two different families of mesoporous silica that were employed as confined space hosts for the synthesis of Pd NPs, SBA-15 and KIT-6, differ in the symmetry of the ordered porous system as well as in the connectivity and tortuosity between pores. Indeed, SBA-15 silica materials are a combined hierarchical micro- and mesoporous material with a two-dimensional (2D) hexagonal pore arrangement (space group *p6mm*). Their porous structure consists of long, parallel cylindrical channels separated from each other, typically slightly curved. Micropores, originating from the hydrophilic chains of the surfactant that penetrate into the silica framework during the synthesis, act as intrawall pores. On the other hand, KIT-6 is characterized by a cubic close-packed bicontinuous pore architecture (space group $Ia\bar{3}d$), organized in a 3D interpenetrating cylindrical porous network. Schematic representations of the pore architecture of SBA-15 and KIT-6, as well as representative TEM micrographs of experimental pristine samples, are shown in Figure 2a,d, together with TEM characterization of the reference sample Aerosil 200 (Figure 2g), investigated as a nonconfining counterpart. The reported micrographs clearly show the above-described regular pore architectures of the two families of mesoporous silica materials and their dramatical difference with respect to the commercial silica sample A200, displaying a mixture of irregularly shaped and sized NPs.

The porous structure of the mesoporous and commercial silica samples, as well as their SSA, total pore volume, and average pore width and pore width distribution, was determined by N_2 physisorption (see Figure 2e for SBA-15 and KIT-6, respectively), confirming the successful synthesis of ordered confined space hosts. In particular, SBA-15 and KIT-6 mesoporous silica samples displayed a Type IV isotherm, typical for mesoporous materials, with Type H1 hysteresis loops for SBA-15 samples, indicating pore channels of constant diameter, and Type H2(a) hysteresis loops for KIT-6 samples, showing also networking effects typical of cubic pore geometry.[22] All four mesoporous supports demonstrated quite narrow mesopore size distributions, as derived by the DFT method.[23] Our results also show that the temperature of the solvothermal treatment in the mesoporous samples' synthetic procedure influences the average pore size, obtaining 7 nm pore size at 80 °C (*A* series of samples) and 9 nm pore size at 120 °C (*C* series of samples) for both mesoporous silica families. On the other hand, the physisorption isotherm of the commercial reference sample A200 (Figure 2h) was identified as a Type II isotherm, typical of macroporous or nonporous samples.[22] Moreover, the SSA of the A200 sample, determined by the BET method,[24] was found to be significantly lower than the SSA of the mesoporous samples, i.e., of about 190 $m^2 \cdot g^{-1}$, compared with SSAs of 750−900 $m^2 \cdot g^{-1}$ determined for the mesoporous silicas (Table 2). These results, combined with the TEM characterization described above, confirmed the commercial sample A200 as a suitable reference support material to be compared with the high-quality-ordered mesoporous silica materials SBA-15 and KIT-6 for evaluation of the space confinement effects on Pd NPs formation and their corresponding catalytic activity.

Pristine mesoporous silica materials were also characterized by low-angle (0.4−6.0° 2θ) and wide-angle (15−90° 2θ) XRD (Figure S5a,b), evidencing crystallinity at the mesoscale level with the associated low-angle region of the diffraction pattern typical of their structure, i.e., hexagonal with space group *p6mm* for SBA-15 and cubic with space group $Ia\bar{3}d$ for KIT-6.

https://doi.org/10.1021/acsanm.4c05689
ACS Appl. Nano Mater. XXXX, XXX, XXX−XXX

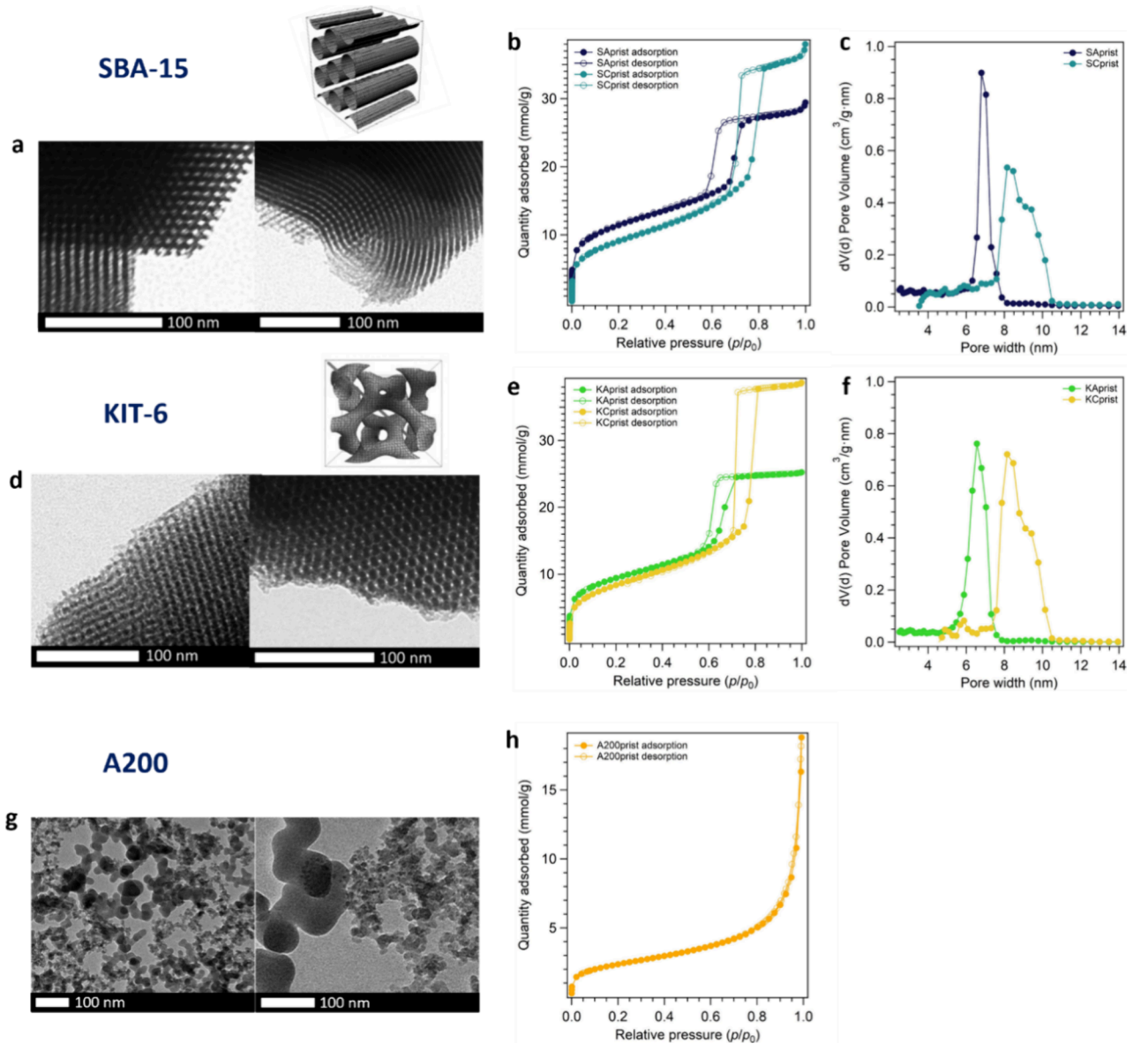

Figure 2. (a) TEM micrographs and schematic representation of the pore system of SBA-15. (b) N_2 physisorption isotherms of the pristine supports *SAprist* (blue lines) and *SCprist* (light-blue lines). (c) Corresponding pore width distribution estimated by the DFT method (NLDFT kernel for silica, −196 °C, cylindrical pores, adsorption branch). (d) TEM micrographs and schematic representation of the pore system of KIT-6. (e) N_2 physisorption isotherms of the pristine supports *KAprist* (green lines) and *KCprist* (yellow lines). (f) Corresponding pore width distribution estimated via the DFT method (NLDFT kernel for silica, −196 °C, cylindrical pores, adsorption branch). (g) TEM micrographs of A200 pristine samples. (h) N_2 physisorption isotherm of the *A200prist* sample (orange line). The adsorption and desorption branch points are reported as filled and empty dots, respectively.

On the other hand, the corresponding wide-angle XRD patterns were characterized by the amorphous bump of silica (about 15−30° 2θ), indicating glass-like disorder in the walls, in agreement with the literature.[25,26] The low-angle region of the XRD patterns of both *A* and *C* series of SBA-15 and KIT-6 materials further confirmed the different pore sizes of the two series: reflection positions were shifted toward lower scattering angles for the *C* series with respect to the *A* series, indicating a larger unit cell parameter (Table 1). Because the unit cell parameter corresponds to the distance between the centers of adjacent mesopores, this result was indicative of a larger combined size, including the pore and wall thicknesses. The unit cell parameter a and pore wall thickness t_{wall} were calculated from the position in d space of the reflections in the low-angle region of the diffractograms and the pore size estimated by DFT from N_2 physisorption (Table 1).[2,27] On the other hand, the low-angle XRD pattern of the commercial A200 sample (Figure S5c) did not display any feature, and the corresponding XRD pattern was characterized by the amorphous halo of silica, indicating the absence of any long- and medium-range structural order, as expected.

Pd NPs on Mesoporous and Nonporous Silica. With the aim of investigating the effect of the spatial confinement offered by the differently sized and interconnected mesopores on the synthesis of supported Pd NPs, the pristine mesoporous materials were employed as hosts and the synthesis of Pd NPs was carried out directly into the pore network of mesoporous silica and, as a reference of the nonconfined sample, on the

https://doi.org/10.1021/acsanm.4c05689
ACS Appl. Nano Mater. XXXX, XXX, XXX−XXX

surface of nonporous silica. A two-step process was performed, encompassing (i) impregnation of the pristine materials with a solution of Pd(II) followed by slow and controlled drying (*impregnated* series) and subsequently (ii) a mild reduction of the impregnated samples (*reduced* series). In particular, the IWI technique, ensuring complete permeation of the impregnating solution (palladium nitrate) into the pores by capillary forces and minimizing the risk of deposition of the precursor material on the outer surface of the support, was employed for the mesoporous catalyst supports. This noble-metal precursor was selected mainly based on its common use for the synthesis of such catalysts because it prevents catalyst contamination with other species (e.g., Cl). By this approach, the role of space confinement on the Pd NPs size, size distribution, and distribution over the support could be appreciated by comparing the results with the reference sample, not displaying any micro- or mesoporosity and likely resulting in an external surface decoration by Pd (i.e., Pd over nonporous silica). A final stoichiometry of 2.0 wt % Pd@SiO_2 was targeted.

To investigate possible changes in the mesoporous structure upon impregnation with a Pd(II) solution, N_2 physisorption and low-angle XRD measurements of the as-prepared impregnated samples were carried out. All of the impregnated mesoporous samples demonstrated that the parent support structures were preserved: Type IV isotherms with Type H1 and Type H2(a) hysteresis loops were observed as their pristine counterpart (see Figures S6 and S7 for the SBA-15 and KIT-6 materials, respectively). However, closure of the hysteresis of SBA-15-impregnated samples occurred at lower relative pressures than the pristine ones, likely indicating the presence of partially blocked mesopores.[22,28] This effect is particularly evident for the *SAimpr* sample. The partial clogging of SBA-15 mesopores could be due to the formation of Pd-based NPs inside/at the entrance of the mesopores. This could be rationalized by taking into account the pore structure of SBA-15, which comprises parallel channels poorly interconnected via disordered micropores. In contrast, the *SCimpr* sample, belonging to the same mesoporous silica family, did not display such marked variation of the hysteresis, likely due to their larger pore size (i.e., 9 vs 7 nm). On the other hand, the highly interconnected mesopore structures of KIT-6 silica supports likely prevented observation of the pore clogging phenomenon in the isotherm even for the sample with the smaller pore size (i.e., *KAimpr*, KIT-6, d_{DFT} = 7 nm). Independent of the hysteresis type, the mean mesopore diameter of all mesoporous supports showed only minor variation after impregnation, demonstrating negligible pore collapse or restructuring following the Pd incorporation procedure (see Figures S6c,f and S7c,f for the DFT pore-size distributions and Table S3 for structural parameters derived from physisorption). Finally, a decrease in the SSA and total pore volume of the mesoporous supports was observed as a result of successful impregnation, as expected (Table S3).

Further evidence that might explain the partial clogging in the case of *SAimpr* is given by the surface species concentrations (Table S4) determined by XPS. The samples with wider pore sizes yielded a surface Pd concentration close to the expected nominal one (2.0 wt % Pd), in particular for *SCimpr*. On the other hand, *SAimpr* showed an increased surface Pd concentration (ca. 4 wt % Pd), which is compatible with a location of the Pd NPs at/close to the entrance of the mesopores, inducing partial clogging.

A comparison of the low-angle region of the diffractograms of Pd(II)-impregnated mesoporous and nonporous silica samples (solid lines) and of the pristine samples (dashed lines), reported in Figure 3a, further demonstrated the successful retention of the parent mesopore architecture of the silica support after impregnation. No significant variation of the cell parameters of pristine and impregnated mesoporous samples was evidenced, indicating that the Pd-based NPs deposited within the mesopores did not significantly affect their long-range order. On the other hand, XRD patterns (Figure 3b) highlighted that impregnation with a $Pd(NO_3)_2$ solution and subsequent mild drying in air led to the formation of PdO NPs, being the strongest and evidently broad (101) reflection of tetragonal PdO clearly recognizable at 34.4° 2θ (space group *I*4/*mmm*, PDF 8-2434) along with the amorphous halo of silica supports. This result was expected because similar results were reported in the literature.[29]

The anticipated oxidized nature of Pd species was also confirmed by XAS investigations at the Pd K-edge (24350 eV). Indeed, a comparison of the white line position of the acquired XANES spectra for the impregnated samples with the spectra of Pd(II) references [i.e., the precursor $Pd(NO_3)_2$ and PdO] and metallic Pd(0), reported in Figure 3d, demonstrated that Pd was present in an oxidized state (2+) in all *impr* samples. Moreover, as expected and confirmed by XRD, the predominant species for all samples was found to be palladium oxide because the XANES and EXAFS features of the impregnated samples closely resembled the XANES and EXAFS profiles of the PdO reference material (the corresponding FT-EXAFS profiles are reported in Figure S9).

To follow the variations in the Pd oxidation state during the reduction step, selected samples (*SAimpr*, *SCimpr*, and *KCimpr*) were treated in conditions similar to those employed in the laboratory (150 °C in 5 vol % H_2/He), while collecting *in situ* Pd K-edge XANES spectra. The XANES spectra of the samples after the reduction step are shown in Figure 3e, together with XANES spectra of the *ex situ* reduced samples *KAred* and *A200red* (not investigated *in situ*) and references spectra. Pronounced differences in the XANES profile were found in comparison with those collected for the impregnated samples (Figure 3d). In particular, the clear change in their near-edge structure was evidenced by the decrease in the white line intensity and shift of the absorption edge to lower energy by about 2 eV, in agreement with the formation of reduced metallic Pd. Small differences in the peak positions and relative intensities (i.e., peak at ca. 24367 eV and shoulder at ca. 24414 eV) with respect to the metallic foil are due to the nanosized dimensions of the NPs.

The fraction of Pd species (i.e., Pd^{2+} and Pd^0) as a function of the temperature during the H_2-TPR measurements was determined by LCF of the measured Pd K-edge XANES spectra using PdO and Pd as reference spectra. The results obtained for the sample *SAimpr* are shown in Figure 3f, while the outcome for the *SCimpr* and *KCimpr* samples is reported in Figure S10, respectively. A very comparable redox behavior of Pd among the catalysts supported over differently sized porous SBA-15 silica was observed: both impregnated samples displayed completely oxidized PdO at room temperature, and the reduction of PdO to Pd was completed at about 140−150 °C. This behavior is in agreement with previous reports also indicating the weak Pd−support interaction in comparison to supports like ceria or zirconia.[30,31] Moreover, a relatively sharp reduction slope was observed because the metallic Pd

https://doi.org/10.1021/acsanm.4c05689
ACS Appl. Nano Mater. XXXX, XXX, XXX−XXX

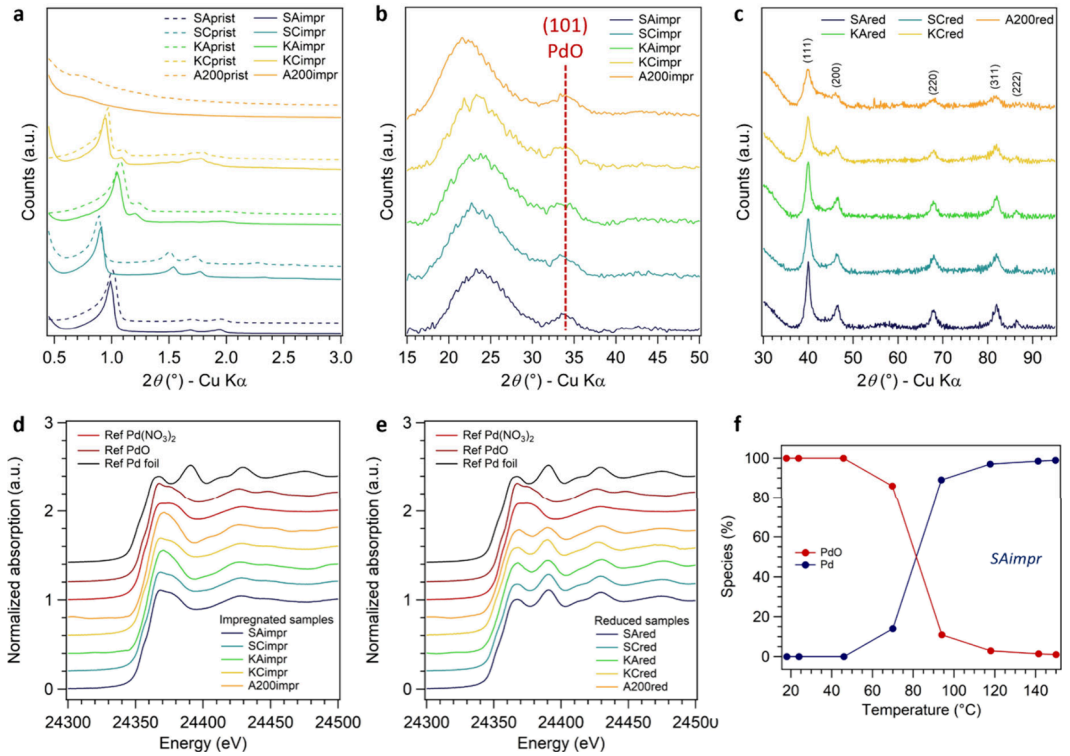

Figure 3. (a) Low-angle and (b) wide-angle XRD patterns of impregnated Pd@SiO_2 (*impr* series, solid lines), compared with low-angle XRD profiles of samples of pristine silica materials (*prist* series, dashed lines). (c) XRD patterns of reduced Pd@SiO_2 samples (*red* series), displaying metallic Pd reflections, marked with the respective Miller indices. (d) Pd K-edge XANES spectra of Pd(II)-impregnated mesoporous and nonporous silica samples and (e) reduced Pd@mesoporous and nonporous silica samples, compared with the reference spectra of $Pd(NO_3)_2$, PdO, and Pd foil. Spectra are shifted vertically for the sake of clarity. For the SBA-15 series and *KCimpr*, spectra collected on granulated fractions are shown. (f) Relative fraction of PdO and Pd species as a function of the temperature obtained by LCF of Pd K-edge XANES spectra of impregnated SBA-15 mesoporous silica with d_{DFT} = 7 nm (*SAimpr*).

species increased significantly over a quite narrow temperature interval. This could possibly indicate homogeneously distributed Pd species on the support, in terms of both size and chemical state.

Finally, the effectiveness of the performed reducing treatment despite the relatively low temperature was further confirmed by XRD characterization. Indeed, the (101) reflection of PdO observed in the *impregnated* series of samples (Figure 3b) was not evidenced in the *reduced* series of samples (Figure 3c). In contrast, the characteristic diffraction patterns of the metallic cubic Pd (space group $Fm\bar{3}m$, PDF 01-1201), along with the previously discussed amorphous halo of silica supports at $2\theta < 30°$, are present. However, the observed metallic Pd reflections are quite broad, consistent with the nanometric crystallite size of Pd species (i.e., 4−6 nm).

The size and size distribution of Pd NPs over the different screened silica supports (*reduced* series) were investigated by HAADF−STEM imaging, and the location of Pd NPs on the silica supports was studied by 3D electron tomography. A comparison of the STEM micrographs of all of the prepared reduced samples is reported in Figure 4, together with histograms showing the Pd NP size distributions. The collected micrographs further confirmed retention of the architecture of both parent mesoporous supports, previously assessed by N_2 physisorption (Type IV isotherms) and low-angle XRD (characteristic patterns of SBA-15 and KIT-6), and the nanometric size of Pd NPs, in agreement with the broad XRD reflections. Moreover, the STEM images confirmed a quite homogeneous distribution of Pd NPs throughout the silica supports for all of the investigated samples. The average size of Pd NPs is in the range of 4.0−5.5 nm, in agreement with the crystallite size estimated by XRD and the reduction properties of the catalysts (XANES-TPR). This size is slightly smaller than that reported by previous studies for analogous Pd/SBA-15 systems (i.e., 4−10 nm, depending on the synthetic conditions).[10,11] For all samples, regardless of the nature of the silica support, the same outcome demonstrates a good degree of control and reproducibility of the IWI technique to produce small nonaggregated supported NPs. Furthermore, it should be noted that the Pd NPs synthesized over mesoporous supports were smaller than those formed over nonporous silica (i.e., 4.0−4.8 vs 5.4 nm; Table 3). Considering the very high-SSA of the mesoporous samples, larger differences in the particle size between Pd NPs supported over mesoporous and nonporous silica could be expected; however, this effect was probably limited due to a poor interaction between the Pd precursor and SiO_2.

Table 3. Mean NPs Size and PDI of Pd NPs Supported on Mesoporous and Nonporous Silica (*Reduced* Series)

	silica support	sample name	mean NPs size [nm]	PDI
mesoporous silica	SBA-15	*SAred*	4.4 ± 1.7	0.39
		SCred	4.8 ± 1.2	0.25
	KIT-6	*KAred*	4.6 ± 1.8	0.39
		KCred	4.0 ± 1.1	0.28
nonporous silica	Aerosil 200	*A200red*	5.4 ± 2.1	0.39

https://doi.org/10.1021/acsanm.4c05689
ACS Appl. Nano Mater. XXXX, XXX, XXX−XXX

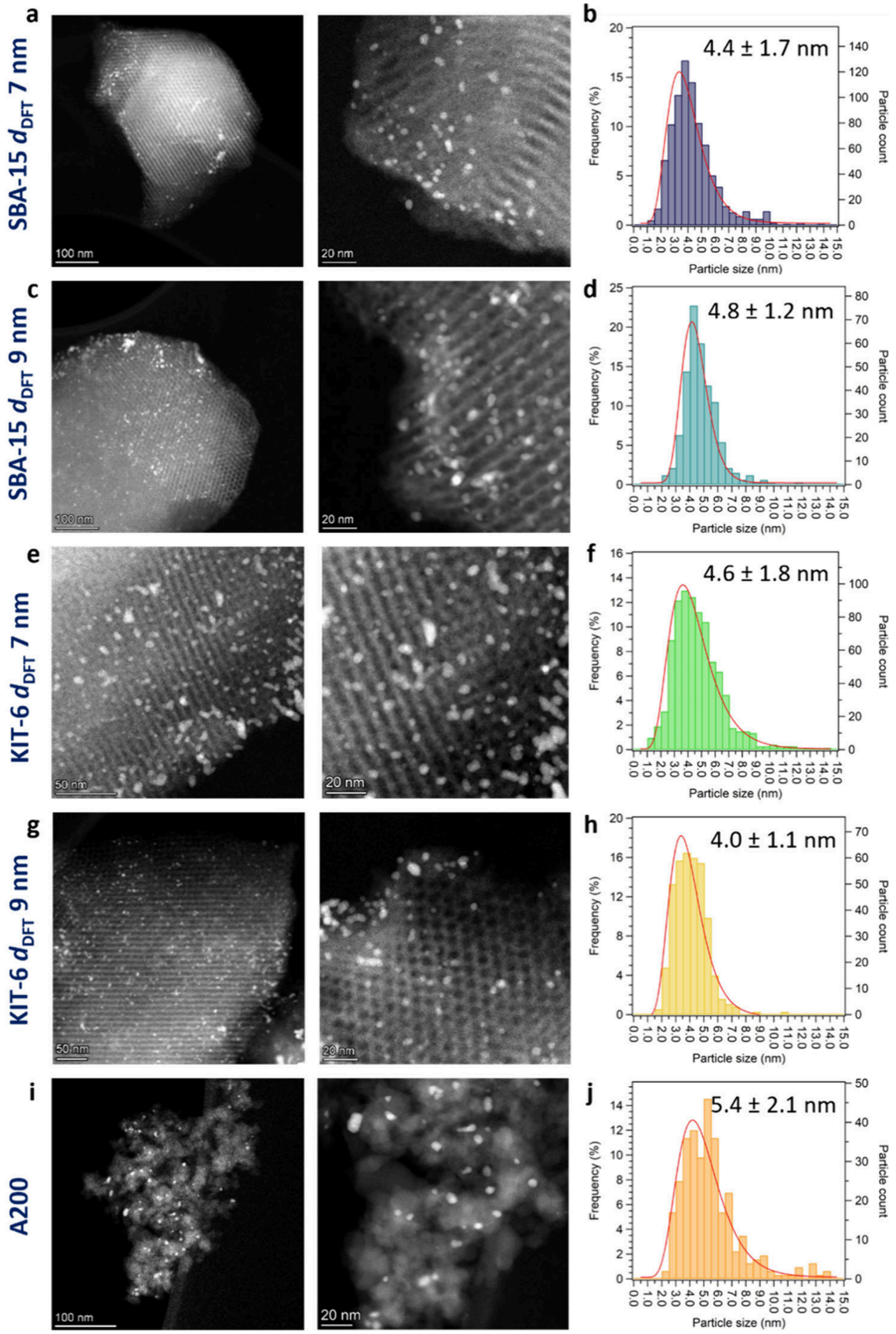

Figure 4. (a, c, e, g, and i) STEM micrographs of Pd NPs (brighter spots, as confirmed by EDX) supported over different silica supports and (b, d, f, h, and j) corresponding histograms reporting the Pd NPs size distribution.

https://doi.org/10.1021/acsanm.4c05689
ACS Appl. Nano Mater. XXXX, XXX, XXX−XXX

Moreover, more outliers (i.e., particles with larger sizes) were found in the size distribution of the nonconfined sample compared with the confined mesoporous ones (Figure 4). This result agrees with the hypothesized space confinement effect exerted by the mesopores of SBA-15 and KIT-6, also offering a higher surface area for deposition as well as possibly leading to a more effective stabilization and/or lower mobility of the NPs over the support. Even though no significant effect of the pore size on the average Pd NPs size was found, because no trend of the NPs dimensions varying with the mesopore diameter was observed, the porous networks with wider diameters seemed to have a positive influence on the NPs size distribution. Actually, among the tested supports, KIT-6 with 9 nm pore size allowed us to obtain the smallest Pd NPs with the narrowest size distribution, thus resulting in the best synthetic control over the NP size and size distribution. Our results suggest that the 3D-interpenetrating and interconnected cylindrical pore structure of KIT-6 likely allows an easier and more homogeneous penetration of the impregnating solution than the parallel independent cylindrical channels of SBA-15, leading to a smaller Pd NPs size with a narrower size distribution.

From the STEM micrographs of the mesoporous silica-supported samples (Figure 4), a significant number of Pd NPs seemed to be located in/along mesopores and/or pore entrances, aimed for, rather than on, external surfaces. In particular, it can be observed that NPs larger than the mean size seem to be on the external surface, while smaller ones are mainly located in the mesopores. However, although in the literature some conclusions about the NPs location were drawn by similar micrographs, even with lower magnification,[10,12,14,32,33] caution must be paid because the STEM micrographs are 2D projections of 3D structures, which can be misleading in determining the Pd NPs location over the support. Thus, electron tomographic measurements were performed to map the distribution of Pd NPs on the selected mesoporous samples. Some representative "slices" from the tomographic reconstructions of mesoporous silica particles supporting Pd NPs are reported in Figures S12−S14 for the *SAred*, *SCred*, and *KCred* samples. From electron tomography, it was found that Pd NPs supported on SBA-15 silica with d_{DFT} of 7 nm (Figure S12) were mostly located on the surface of the silica particle or around the entrance of the pores, in agreement with the N_2 physisorption results, indicating partial clogging of the mesopores. It could thus be hypothesized that the 7-nm-wide cylindrical nonconnected mesopores did not enable an efficient capillary penetration of the precursor solution or did not limit its migration during the drying process, leaving the precursor mainly deposited at their entrance. On the other hand, when SBA-15 silica with a larger pore diameter (d_{DFT} = 9 nm) was employed as the support and confined environment, Pd NPs were easily found in the inner structure of the mesoporous matrix (Figure S13), indicating an effective nucleation of Pd nanostructures in the confined space of the mesopores. This result confirmed the findings outlined from physisorption data, not displaying any significant clogging while showing a larger decrease in the total pore volume after impregnation (−17% vs −4%; Table S3), and can most likely be rationalized by considering the larger pore size of the *SCprist* sample with respect to the *SAprist* sample. Finally, it is worth noting the more effective confinement of the synthesis of Pd NPs inside the cylindrical parallel mesopores of SBA-15 with larger pore size resulted in a slightly larger size (4.8 vs 4.4 nm) but a narrower size distribution of Pd NPs [polydispersity index (PDI) of 0.25 vs 0.39; Table 3] and thus a more controlled synthetic outcome. Last, tomographic investigation of the sample supported over KIT-6 (d_{DFT} = 9 nm; Figure S14) demonstrated that the highly interconnected mesoporous architecture of KIT-6 allowed facile and effective percolation and incorporation of the Pd precursor into the mesopores, resulting in the largest decrease in total pore volume after impregnation (Table S3) and in a quite homogeneous distribution of Pd NPs after drying and reduction. The *KCred* sample also ended up being characterized by the smallest average size of Pd NPs with narrow size distribution, indicating optimal synthetic control.

Pd NPs on Mesoporous and Nonporous Silica as Catalysts for CO Oxidation. *Catalytic Activity toward CO Oxidation of Pd NPs Supported on Mesoporous and Nonporous Silica.* Finally, Pd NPs supported on mesoporous and nonporous silica materials were tested as heterogeneous catalysts for the oxidation of carbon monoxide, chosen as the model reaction for the catalytic oxidative reactions (see the Experimental Section for technical details). The conversion curves of CO as a function of the temperature over Pd-based catalysts supported on KIT-6 mesoporous silica with pore sizes of 7 and 9 nm are reported as examples in Figure 5a−d, while conversion curves for Pd NPs supported on SBA-15 and nonporous silica, displaying analogous behavior, are shown in Figures S15 and S16, respectively. During the light-off, three regions of activity were observed: (i) low-activity region (about 50−150 °C), corresponding to the temperature range in which the reaction is kinetically controlled: at low temperatures, CO has been reported to inhibit reaction due to its strong adsorption on large PdO_x clusters and particles[34] (vide infra); (ii) high-activity region, coinciding with the temperature range in which the conversion curve is steeper (about 150−200 °C): the reaction is controlled by the surface reaction of CO and adsorbed oxygen including possible diffusion of the reactive mixture into porous supports;[35] (iii) a stability region (>200 °C), where the conversion is complete and reaches a plateau. When considering the light-out curve, the formation of a normal hysteresis profile was noted: the ascending (light-off) and descending (light-out) branches of the CO conversion versus temperature plot did not coincide, and, in particular, the catalytic activity during the heating process occurred at a higher temperature than that during the cooling process. This behavior is quite common for CO oxidation and many other oxidation exothermic reactions using Pd- or Pt-based catalysts, such as CO, NO, C_3H_6, and CH_4 oxidations.[36−42] However, its origin is still controversial, and it has been discussed from both a macroscopic (e.g., mass and heat diffusion effects) or microscopic (e.g., mechanistic and structural aspects) perspective. In particular, it was ascribed to the strong exothermicity and local overheating of the active sites, releasing heat at the surface of the catalyst and determining a surface temperature higher than the reactor temperature: in this way, the catalyst remains active also at lower temperatures during cooling. In addition, the hysteresis origin has been associated with the multiplicity of steady states, preferential surface coverage with reactive gases, oxidation of the catalyst, and temperature fluctuations.[39,43,44]

The temperature at which 50% of CO conversion (i.e., T_{50}) was achieved during the light-off step, shown in Figure 5e, was employed as a parameter to compare the catalytic activity of the five catalysts among themselves and among different

https://doi.org/10.1021/acsanm.4c05689
ACS Appl. Nano Mater. XXXX, XXX, XXX−XXX

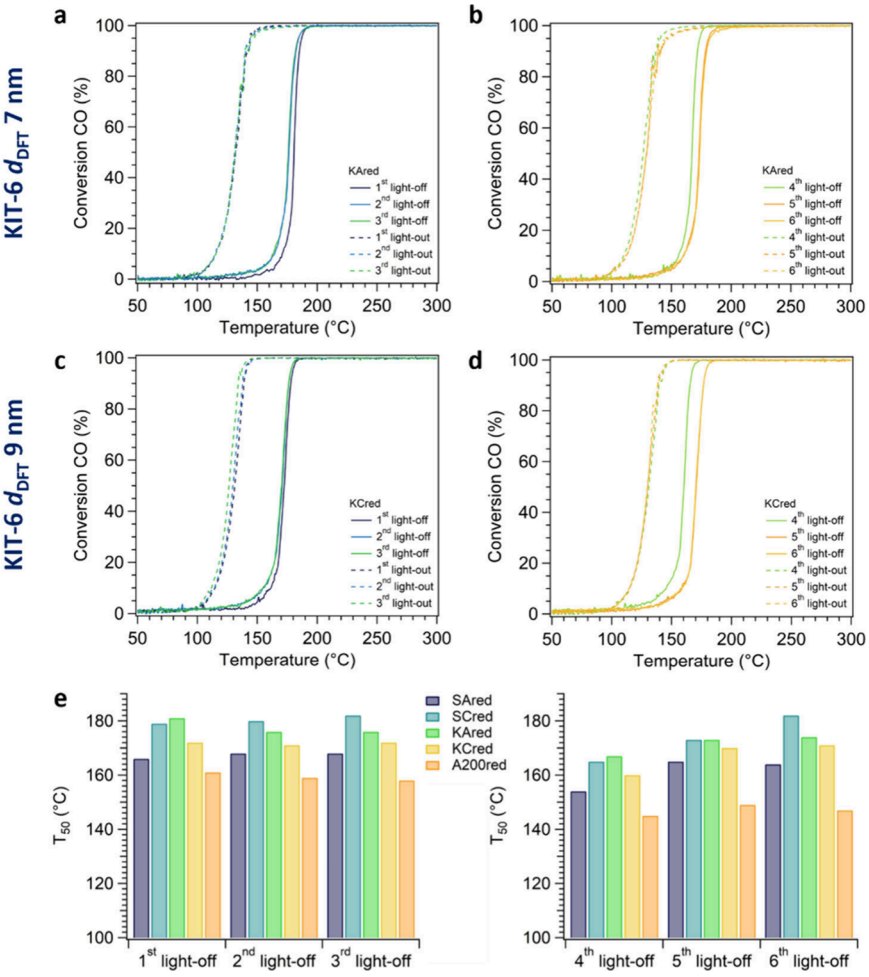

Figure 5. Catalytic conversion curves of Pd NPs on KIT-6 mesoporous silica, with pore sizes of 7 nm (a and b, the *KAred* sample) and 9 nm (c and d, the *KCred* sample), acquired before (1st, 2nd, and 3rd cycles; a and c) and after (4th, 5th, and 6th cycles; b and d) the *in situ* reduction step. (e) Comparison of T_{50} for CO oxidation light-off cycles on different Pd/SiO_2 catalysts, acquired before (1st, 2nd, and 3rd cycles) and after (4th, 5th, and 6th cycles) the *in situ* reduction step.

consecutive cycles, given the similarities in the shape of the conversion curves. Generally, T_{50} values in the 145−182 °C range were obtained, comparable to or lower than the values reported in the literature for analogous Pd/SiO_2 catalysts (about 140−280 °C).[10,36,45] A clear variation of the T_{50} values according to the microstructural features of the silica support was observed, following the trend KIT-6 (d_{DFT} = 7 nm) ≈ SBA-15 (d_{DFT} = 9 nm) > KIT-6 (d_{DFT} = 9 nm) > SBA-15 (d_{DFT} = 7 nm) > A200 for each catalytic cycle, whereas the Pd NPs size does not appear to play a consistent role. Indeed, Pd NPs supported on nonporous silica were found to be the more active catalysts for CO oxidation, possibly because 2 wt % Pd NPs on nonporous silica were deposited over a considerably smaller surface area: the *A200red* sample was characterized by a higher superficial concentration of Pd per unit area than its mesoporous counterparts (i.e., about 0.07 vs 0.03−0.04 $mg_{Pd}\cdot m^{-2}$, values calculated based on the BET and XPS data in Tables S3 and S4, respectively). This factor, ultimately affecting the distance between Pd NPs and thus the heat distribution during the exothermic reaction, could likely influence their catalytic activity, as reported in the literature.[46] However, these differences in activity cannot be solely explained in terms of differences in the concentration of Pd per unit area because the values determined by XPS do not correlate directly with the catalytic activity. Among mesoporous samples, the best catalytic performance was shown by Pd NPs on SBA-15 mesoporous silica with a mesopore diameter of 7 nm, and this observation, analogous to the nonporous sample, could agree with the presence of Pd NPs mostly on the outer surface of the support and at the entrance of the pores, as demonstrated by N_2 physisorption and electron tomography measurements, thus with a localized higher superficial concentration of Pd NPs. On the other hand, Pd NPs inside mesopores of SBA-15 and KIT-6 silica, whose locations were demonstrated by electron tomography, were found to be less active for CO oxidation possibly because diffusion of the reactive gases was ruled by the geometrical porous systems.[47] In particular, Pd NPs synthesized in 9-nm-sized mesopores of KIT-6, with a smaller size and a narrower size distribution (Table 3), displayed a lower light-off temperature, while a less marked difference was found between the T_{50} values of Pd NPs supported on SBA-15 (d_{DFT} = 9 nm) and KIT-6 (d_{DFT} = 7 nm), in agreement with their comparable size and size distribution (Table 3).

Because the light-off temperature of the samples over the first three different consecutive catalytic cycles was observed to be quite constant (Figure 5e), good stability of the samples and nonsignificant deactivation of the catalyst can be concluded.

https://doi.org/10.1021/acsanm.4c05689
ACS Appl. Nano Mater. XXXX, XXX, XXX−XXX

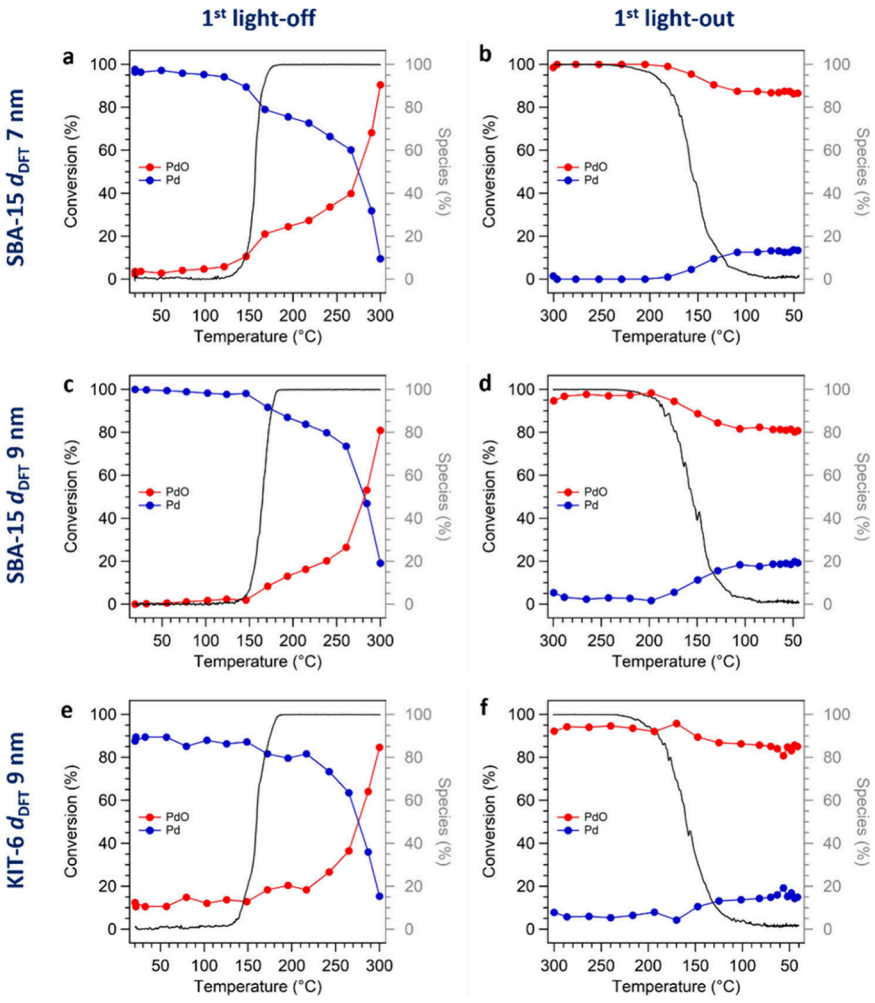

Figure 6. CO conversion profile during the first light-off (a, c, and e) and light-out (b, d, and f) of three different samples (*SAred*, *SCred*, and *KCred* in parts a and b, c and d, and e and f, respectively), compared with the evolution of the relative fraction of Pd species (Pd and PdO, blue and red curves, respectively) during catalytic activity, obtained by LCF of the Pd K-edge XANES spectra.

However, after the *in situ* reduction step, performed between the third and fourth catalytic cycles, a significant increase in the catalytic activity of all samples was evidenced, ascribable to the efficient removal of adsorbed oxygen/hydroxyl and other moieties from the surface of the catalyst, exposing the active sites (in the reduced state) to fresh adsorbates and therefore to the efficient reactivation of the catalyst.[48,49] The beneficial effect of this activation is only temporary because the ignition curves fall back, in further cycles, to the values before the reduction step, possibly due to reoxidation of the NPs surface.

Operando XAS Analysis. In order to unveil the relationship between the catalytic activity of Pd NPs supported on different silica supports and the oxidation state changes of Pd during CO oxidation, *operando* XAS measurements were performed at the Pd K-edge (24350 eV) for selected samples (*SAimpr*, *SCimpr*, and *KCimpr*). Indeed, *operando* XAS has been proven to be extraordinarily successful in investigating the atomic structure and oxidation state of heterogeneous catalysts under operative conditions and determining structure−activity correlations.[50−54] In particular, the impregnated samples were first treated in a reducing atmosphere (TPR, as discussed above) to obtain *in situ* the reduced samples. Subsequently, the reduced catalysts underwent two consecutive light-off/light-out cycles under a reactive oxidative atmosphere (1000 ppm of CO, 10% O_2, and He balance), to test their catalytic activity under transient conditions comparable to those employed in laboratory testing. During the catalytic tests, the Pd K-edge XAS spectrum of the samples was simultaneously acquired (*operando* measurements), and the relative percentage of Pd^{2+} and Pd species as a function of the temperature during CO oxidation was estimated through LCF of the XANES spectra.

Figure 6 shows the CO conversion profile during the first catalytic cycle, together with the simultaneous evolution of the relative fraction of Pd species for the investigated samples (second catalytic cycle in Figure S17). First of all, the laboratory catalytic and *operando* tests were observed to be comparable because the light-off temperatures estimated with the two setups were found to be similar, in terms of both absolute T_{50} values and the overall activity of the samples, following the previously reported T_{50} trend of SBA-15 (d_{DFT} = 9 nm) > KIT-6 (d_{DFT} = 9 nm) > SBA-15 (d_{DFT} = 7 nm). Interestingly, it was observed that the onset of CO conversion occurs simultaneously or is immediately followed by PdO formation: during the first light-off (Figure 6a,c,e), the oxidation of metallic Pd (blue lines) to PdO (red lines, oxidic species) began at ca. 130−150 °C, followed concurrently by ignition of the CO conversion. Even though an incomplete oxidation of Pd to PdO was observed at the end of the light-off

https://doi.org/10.1021/acsanm.4c05689
ACS Appl. Nano Mater. XXXX, XXX, XXX−XXX

Table 4. Mean NPs Size and PDI of Pd NPs Supported on Mesoporous and Nonporous Silica (*Reduced* Series) after Catalytic Testing and Their Relative Percentage Increase with Respect to the Estimated Values Prior to Catalytic Tests

	silica support	sample name	mean NPs size [nm]	increase in the NPs size [%][a]	PDI	increase in the PDI [%][b]
mesoporous silica	SBA-15	*SAred*	5.3 ± 2.8	20	0.52	33
		SCred	4.5 ± 1.6		0.36	44
	KIT-6	*KAred*	5.7 ± 2.8	24	0.49	26
		KCred	5.2 ± 2.2	30	0.42	50
nonporous silica	Aerosil 200	*A200red*	6.4 ± 2.4	19	0.38	

[a]Calculated as $(d_{\text{Pd postcatalysis}} - d_{\text{Pd precatalysis}}) \times 100/d_{\text{Pd precatalysis}}$. [b]Calculated as $(\text{PDI}_{\text{Pd postcatalysis}} - \text{PDI}_{\text{Pd precatalysis}}) \times 100/\text{PDI}_{\text{Pd precatalysis}}$.

cycle (about 80−90% PdO at 300 °C), it was completed during the dwell step at 300 °C (5 min), i.e., before starting the cooling ramp (light-out), for samples supported over SBA-15 silica; conversely, about 5% of the Pd supported over KIT-6 mesoporous silica remained reduced. On the other hand, during the light-out (Figure 6b,d,f), a partial reduction of PdO to Pd was observed (about 15−20% of the total Pd species). On the prereduced Pd NPs, the reaction is expected to proceed according to the Langmuir−Hinshelwood dual-site mechanism, involving a first step of competitive chemisorption of CO and O_2 onto an adsorption site of the metallic surface of the catalyst (with the CO chemisorption favored at low temperatures), followed by their reaction and production of CO_2, which eventually desorbs as the product.[55,56] However, once PdO_x species are formed, CO oxidation most probably proceeds via the Mars−Van Krevelen mechanism, involving the reduction and reoxidation of Pd species. Such a mechanism is plausible, especially for the following light-off/light-out cycles, because most Pd species are in an oxidized state at the end of the first light-off/light-out cycle. Such a mechanism has been proposed previously by several research groups for Pd-based CO oxidation catalysts.[36,57−59]

In agreement with the laboratory results obtained for the reductively treated catalysts, the second light-offs, shown in Figure S17, are shifted toward higher temperatures for all samples. This indicates a decrease in the catalytic activity, which can be correlated to the above-mentioned structural changes. No further major variations in the noble-metal structure occurred, and the oxidized Pd (PdO) was consistently the predominant species during the second light-off/light-out cycle. Hence, whereas the presence of sub-stoichiometric $PdO_{x<1}$ species (i.e., oxygen-covered metallic Pd NPs) is highly beneficial because this represents the active phase in the CO conversion reaction, PdO formed via bulk oxidation of the noble-metal NPs seems to be considerably less active, as was also previously reported in the literature.[60] Nonetheless, variations in the relative percentage of Pd species were found, similar to the first catalytic cycle: during the light-off, an increase in the PdO relative fraction was observed, corresponding to the start of CO conversion, while a partial reduction occurred during the light-out step. In particular, after the second light-out, a lower percentage of reduced Pd was observed with respect to the first light-out, i.e., about 10% vs 15−20%, showing the progress of bulk oxidation and the increased stability of PdO species toward reduction by CO. Relative percentages of the different Pd species at the beginning and end of each light-off and light-out are reported in Table S5. Overall, the observed trend in the catalytic activity of the investigated Pd samples seems to be due to the interplay of multiple factors that are involved in the studied process, e.g., (i) Pd NPs size, (ii) size distribution, (iii) distribution over the support, (iv) Pd NPs accessibility and external surface concentration, (v) Pd oxidation state variation, and (vi) pore-size distribution and connectivity.

Samples after Catalysis. To indeed verify if the Pd NPs' size, size distribution, and distribution over silica supports underwent modifications as a consequence of the catalytic tests, the samples were characterized by STEM after complete catalytic cycle treatment (following the testing procedure reported in Figure S2). In particular, because Pd NPs and the inert silica support do not interact strongly, Pd NPs can migrate on the surface. A comparison of representative STEM micrographs of the samples after catalytic tests is reported in Figure S18, together with histograms showing the Pd NPs' size distributions. The collected micrographs further confirmed the retention of the architecture of both parent mesoporous supports upon subsequent heating treatments up to 300 °C. However, the size and size distribution of Pd NPs, reported in Table 3, were found to be affected by the performed catalytic tests due to slightly larger NPs with a broader size distribution compared with the state before the catalytic tests (Table 4) were observed. In particular, some larger Pd aggregates were found over KIT-6 (d_{DFT} = 7 nm) and SBA-15 (d_{DFT} = 7 nm). Noticeably, the catalyst supported over other mesoporous supports demonstrated instead a smaller increase in the average Pd NPs size upon aging and under catalytic conditions. Considering the relatively low temperature employed for the catalytic tests (i.e., 300 °C) and short dwell time, the sintering of Pd NPs is expected to be minor. In line with the *operando* XAS data, the observed increase in the particle size after the catalytic reaction is most probably a consequence of the change in the oxidation state of Pd because lattice expansion could occur due to PdO formation. Hence, excluding the change in the oxidation state, a relatively good stability toward aggregation is shown by the Pd NPs deposited on mesoporous silica supports within the temperature window applied in this study for the catalytic tests.

■ CONCLUSIONS

In this work, the synthesis of Pd NPs in the confined space of 7- and 9-nm-sized mesopores of two families of mesoporous silica materials (SBA-15 and KIT-6) was systematically investigated as a function of different support materials. The confined synthesis outcomes were compared with a reference sample of Pd NPs synthesized on the outer surface of a nonporous silica material counterpart to evaluate the effect of the spatial confinement offered by differently sized and interconnected mesopores with different arrangement and accessibility on the size and size distribution of the supported NPs and on their distribution over the support. The outcome of our study shows that mesopore spatial constraint was effective in obtaining slightly smaller and more narrowly distributed Pd NPs (i.e., 4.0−4.8 nm) with respect to nonporous silica (i.e., 5.4 nm), located mainly within the

https://doi.org/10.1021/acsanm.4c05689
ACS Appl. Nano Mater. XXXX, XXX, XXX−XXX

pore systems (electron tomography), while retaining the mesoporous support architectures (N_2 physisorption and low-angle XRD). However, despite the fact that the effectiveness of the employed synthetic approach could be demonstrated in confining the synthesis of Pd NPs within 9-nm-sized SBA-15 parallel cylindrical mesopores and the more interconnected 3D structure of KIT-6, the N_2 physisorption measurements evidenced the partial clogging of SBA-15 parallel channels when employing the support with a smaller diameter (i.e., 7 nm). The accessibility of Pd species and their stability were probed by CO oxidation in comparison to a nonporous reference sample. This was further substantiated by *operando* XAS investigations, which uncovered the dynamic change in the Pd state as a function of CO conversion, ultimately leading to a stable catalyst state. Oxidized Pd species were found to be the active phase of the catalytic reaction, but a complex interplay of several factors concurs in regulating the catalytic activity of the supported NPs. Hence, further studies on the impact of the noble-metal precursor and deposition method as well as the pretreatment conditions need to be further screened to optimize the noble-metal particle size and distribution and correlate them with the resulting activity.

■ ASSOCIATED CONTENT

Data Availability Statement

STEM and tomography data (also as videos) that support the findings are openly available at the following link: 10.35097/cmWzAfxcTZsOFisw.

Supporting Information

The Supporting Information is available free of charge at https://pubs.acs.org/doi/10.1021/acsanm.4c05689.

> Additional experimental details and schemes, additional XRD patterns and N_2 physisorption isotherms, surface species concentration derived from XPS, FT-EXAFS, LCF of Pd K-edge XANES during TPR, tomography Z slices, additional catalytic conversion curves, LCF of Pd K-edge XANES during CO conversion, and STEM images after catalytic testing with size analysis (PDF)

■ AUTHOR INFORMATION

Corresponding Author

Silvia Gross − *Dipartimento di Scienze Chimiche, Università degli Studi di Padova, Padova 35131, Italy; Institut für Technische Chemie und Polymerchemie, Karlsruher Institut für Technologie (KIT), Karlsruhe 76131, Germany;* orcid.org/0000-0003-1860-8711; Email: silvia.gross@unipd.it

Authors

Francesca Tajoli − *Dipartimento di Scienze Chimiche, Università degli Studi di Padova, Padova 35131, Italy;* orcid.org/0000-0002-6416-6638

Paolo Dolcet − *Dipartimento di Scienze Chimiche, Università degli Studi di Padova, Padova 35131, Italy; Institut für Technische Chemie und Polymerchemie, Karlsruher Institut für Technologie (KIT), Karlsruhe 76131, Germany;* orcid.org/0000-0001-9583-9375

Sarah Claas − *Institute of Inorganic and Applied Chemistry, University of Hamburg, Hamburg 20146, Germany;* orcid.org/0009-0004-2144-1822

Carina B. Maliakkal − *Institut für Nanotechnologie (INT), Karlsruher Institut für Technologie (KIT), Eggenstein-Leopoldshafen 76344, Germany*

Di Wang − *Institut für Nanotechnologie (INT), Karlsruher Institut für Technologie (KIT), Eggenstein-Leopoldshafen 76344, Germany; Karlsruhe Nano Micro Facility (KNMFi), Karlsruher Institut für Technologie (KIT), Eggenstein-Leopoldshafen 76344, Germany;* orcid.org/0000-0001-9817-7047

Christian Kübel − *Institut für Nanotechnologie (INT), Karlsruher Institut für Technologie (KIT), Eggenstein-Leopoldshafen 76344, Germany; Karlsruhe Nano Micro Facility (KNMFi), Karlsruher Institut für Technologie (KIT), Eggenstein-Leopoldshafen 76344, Germany;* orcid.org/0000-0001-5701-4006

Maria Casapu − *Institut für Technische Chemie und Polymerchemie, Karlsruher Institut für Technologie (KIT), Karlsruhe 76131, Germany;* orcid.org/0000-0002-8755-9856

Michael Fröba − *Institute of Inorganic and Applied Chemistry, University of Hamburg, Hamburg 20146, Germany*

Jan-Dierk Grunwaldt − *Institut für Technische Chemie und Polymerchemie, Karlsruher Institut für Technologie (KIT), Karlsruhe 76131, Germany; Institut für Katalyseforschung und -technologie, Karlsruher Institut für Technologie (KIT), Eggenstein-Leopoldshafen 76344, Germany;* orcid.org/0000-0003-3606-0956

Complete contact information is available at: https://pubs.acs.org/10.1021/acsanm.4c05689

Author Contributions

The manuscript was written through contributions of all authors. All authors have given approval to the final version of the manuscript.

Funding

Project P-DiSC-2018 "Space matters: crystallization of inorganic nanostructures in confined spaces" (Dipartimento di Scienze Chimiche, Università degli Studi di Padova); SFB Project CRC 1441 "TrackAct" (Project-ID 426888090); KIT (Karlsruhe Institute of Technology); MIUR (Ministero dell'Istruzione, dell'Università e della Ricerca); TEM instrument time (Proposal ID 2022-027-031257) funded by KNMFi; synchrotron beamtime (Proposal ID 20211613) funded by SOLEIL.

Notes

The authors declare no competing financial interest.

■ ACKNOWLEDGMENTS

SOLEIL Synchrotron is acknowledged for providing synchrotron radiation facilities (Proposal ID 20211613). Dr. Emiliano Fonda (SAMBA beamline, SOLEIL Synchrotron) is kindly acknowledged for technical assistance during the beamtime. F.T. and S.G. acknowledge the DiSC Project P-DiSC-2018 "Space matters: crystallization of inorganic nanostructures in confined spaces". F.T. acknowledges MIUR and Ph.D. School in Molecular Sciences (Department of Chemical Sciences, University of Padova) for funding. Finally, we thank the DFG within CRC1441 for support (Project ID 426888090). F.T. gratefully thanks Prof. Jan-Dierk Grunwaldt for supporting her staying at KIT. S.G. warmly thanks the DFG and the SFB Project CRC 1441 "TrackAct" for the provision of a Mercator Fellow position at KIT and the University of Padova. We

gratefully thank the PanLab department facility (Department of Chemical Sciences, University of Padova), funded by the MIUR "Dipartimenti di Eccellenza" Grant NExuS. Federico Caicci is acknowledged for TEM images of the pristine A200 sample. C.B.M. acknowledges Dr. Xiaohui Huang, who was then at KIT, for teaching tomography. S.C. and M.F. thank the Department of Electron Microscopy at the University of Hamburg for TEM images of pristine mesoporous supports and Sandra König from the University of Hamburg for gas physisorption measurements of pristine mesoporous supports. Thomas J. Eldridge from KIT is acknowledged for supporting gas physisorption measurements.

■ ABBREVIATIONS

BET, Brunauer–Emmett–Teller; DFT, density functional theory; EDX, energy-dispersive X-ray spectroscopy; EXAFS, extended X-ray absorption fine structure; FTIR, Fourier transform infrared; HAADF-STEM, high-angle annular dark-field scanning transmission electron microscopy; IWI, incipient wetness impregnation; LCF, linear combination fitting; MFC, mass flow controller; NLDFT, nonlocalized density functional theory; NP, nanoparticle; PDI, polydispersity index; SSA, specific surface area; TEM, transmission electron microscopy; TEOS, tetraethyl orthosilicate; TPR, temperature-programmed reduction; XANES, X-ray absorption near-edge structure; XAS, X-ray absorption spectroscopy; XPS, X-ray photoelectron spectroscopy; XRD, X-ray diffraction; WHSV, weight hourly space velocity

■ REFERENCES

(1) McNaught, A. D.; Wilkinson, A. *IUPAC Compendium of Chemical Terminology (the "Gold Book")*, 2nd ed.; Blackwell Scientific Publications: Oxford, U.K., 1997.

(2) Ciesla, U.; Schüth, F. Ordered Mesoporous Materials. *Microporous Mesoporous Mater.* **1999**, *27* (2–3), 131–149.

(3) Corma, A. From Microporous to Mesoporous Molecular Sieve Materials and Their Use in Catalysis. *Chem. Rev.* **1997**, *97* (6), 2373–2420.

(4) Laursen, A. B.; Højholt, K. T.; Lundegaard, L. F.; Simonsen, S. B.; Helveg, S.; Schüth, F.; Paul, M.; Grunwaldt, J.-D.; Kegnæs, S.; Christensen, C. H.; Egeblad, K. Substrate Size-Selective Catalysis with Zeolite-Encapsulated Gold Nanoparticles. *Angew. Chem., Int. Ed.* **2010**, *49* (20), 3504–3507.

(5) Moller, K.; Bein, T. Inclusion Chemistry in Periodic Mesoporous Hosts. *Chem. Mater.* **1998**, *10* (10), 2950–2963.

(6) Wu, S.-H.; Mou, C.-Y.; Lin, H.-P. Synthesis of Mesoporous Silica Nanoparticles. *Chem. Soc. Rev.* **2013**, *42* (9), 3862.

(7) Trovarelli, A.; Llorca, J. Ceria Catalysts at Nanoscale: How Do Crystal Shapes Shape Catalysis? *ACS Catal.* **2017**, *7* (7), 4716–4735.

(8) Al Soubaihi, R.; Saoud, K.; Dutta, J. Critical Review of Low-Temperature CO Oxidation and Hysteresis Phenomenon on Heterogeneous Catalysts. *Catalysts* **2018**, *8* (12), 660–678.

(9) Zhou, Y.; Wang, Z.; Liu, C. Perspective on CO Oxidation over Pd-Based Catalysts. *Catal. Sci. Technol.* **2015**, *5* (1), 69–81.

(10) Wang, H.; Liu, C. Preparation and Characterization of SBA-15 Supported Pd Catalyst for CO Oxidation. *Appl. Catal. B Environ.* **2011**, *106* (3–4), 672–680.

(11) Liu, C.-H.; Lin, C.-Y.; Chen, J.-L.; Lu, K.-T.; Lee, J.-F.; Chen, J.-M. SBA-15-Supported Pd Catalysts: The Effect of Pretreatment Conditions on Particle Size and Its Application to Benzyl Alcohol Oxidation. *J. Catal.* **2017**, *350*, 21–29.

(12) Morère, J.; Tenorio, M. J.; Torralvo, M. J.; Pando, C.; Renuncio, J. A. R.; Cabañas, A. Deposition of Pd into Mesoporous Silica SBA-15 Using Supercritical Carbon Dioxide. *J. Supercrit. Fluids* **2011**, *56* (2), 213–222.

(13) Wang, Z.; Xie, Y.; Liu, C. Synthesis and Characterization of Noble Metal (Pd, Pt, Au, Ag) Nanostructured Materials Confined in the Channels of Mesoporous SBA-15. *J. Phys. Chem. C* **2008**, *112* (50), 19818–19824.

(14) Parlett, C. M. A.; Bruce, D. W.; Hondow, N. S.; Newton, M. A.; Lee, A. F.; Wilson, K. Mesoporous Silicas as Versatile Supports to Tune the Palladium-Catalyzed Selective Aerobic Oxidation of Allylic Alcohols. *ChemCatChem.* **2013**, *5* (4), 939–950.

(15) Speil, N.; Hoffmann, F.; Brieler, F. J.; Fröba, M. From the Outside to the inside: Elucidation of the Mechanism of Pseudomorphic Transformation of SBA-15 into MCM-41 by Following Its Time-Resolved Conversion. *Microporous Mesoporous Mater.* **2021**, *328*, 111442.

(16) Kleitz, F.; Hei Choi, S.; Ryoo, R. Cubic Ia3d Large Mesoporous Silica: Synthesis and Replication to Platinum Nanowires, Carbon Nanorods and Carbon Nanotubes. *Chem. Commun.* **2003**, No. 17, 2136.

(17) Rouquerol, J.; Avnir, D.; Everett, D. H.; Fairbridge, C.; Haynes, M.; Pernicone, N.; Ramsay, J. D. F.; Sing, K. S. W.; Unger, K. K. Guidelines for the Characterization of Porous Solids. *Characterization of Porous Solids III*; Elsevier, 1994; Vol. *87*, pp 1–9. DOI: 10.1016/S0167-2991(08)63059-1.

(18) Schindelin, J.; Arganda-Carreras, I.; Frise, E.; Kaynig, V.; Longair, M.; Pietzsch, T.; Preibisch, S.; Rueden, C.; Saalfeld, S.; Schmid, B.; Tinevez, J. Y.; White, D. J.; Hartenstein, V.; Eliceiri, K.; Tomancak, P.; Cardona, A. Fiji: An Open-Source Platform for Biological-Image Analysis. *Nat. Methods* **2012**, *9* (7), 676–682.

(19) Schneider, C. A.; Rasband, W. S.; Eliceiri, K. W. NIH Image to ImageJ: 25 Years of Image Analysis. *Nat. Methods* **2012**, *9* (7), 671–675.

(20) La Fontaine, C.; Belin, S.; Barthe, L.; Roudenko, O.; Briois, V. ROCK: A Beamline Tailored for Catalysis and Energy-Related Materials from Ms Time Resolution to Mm Spatial Resolution. *Synchrotron Radiat. News* **2020**, *33* (1), 20–25.

(21) Landrot, G. FASTOSH: A Software to Process XAFS Data for Geochemical & Environmental Applications. *Goldschmidt Abstracts*; 2018; Vol. *1402*.

(22) Thommes, M.; Kaneko, K.; Neimark, A. V.; Olivier, J. P.; Rodriguez-Reinoso, F.; Rouquerol, J.; Sing, K. S. W. Physisorption of Gases, with Special Reference to the Evaluation of Surface Area and Pore Size Distribution (IUPAC Technical Report). *Pure Appl. Chem.* **2015**, *87* (9–10), 1051–1069.

(23) Landers, J.; Gor, G. Y.; Neimark, A. V. Density Functional Theory Methods for Characterization of Porous Materials. *Colloids Surfaces A Physicochem. Eng. Asp.* **2013**, *437*, 3–32.

(24) Brunauer, S.; Emmett, P. H.; Teller, E. Adsorption of Gases in Multimolecular Layers. *J. Am. Chem. Soc.* **1938**, *60* (2), 309–319.

(25) Zhao, D.; Feng, J.; Huo, Q.; Melosh, N.; Fredrickson, G. H.; Chmelka, B. F.; Stucky, G. D. Triblock Copolymer Syntheses of Mesoporous Silica with Periodic 50 to 300 Angstrom Pores. *Science* **1998**, *279* (5350), 548–552.

(26) Cassiers, K.; Linssen, T.; Mathieu, M.; Benjelloun, M.; Schrijnemakers, K.; Van Der Voort, P.; Cool, P.; Vansant, E. F. A Detailed Study of Thermal, Hydrothermal, and Mechanical Stabilities of a Wide Range of Surfactant Assembled Mesoporous Silicas. *Chem. Mater.* **2002**, *14* (5), 2317–2324.

(27) Ravikovitch, P. I.; Neimark, A. V. Relations between Structural Parameters and Adsorption Characterization of Templated Nanoporous Materials with Cubic Symmetry. *Langmuir* **2000**, *16* (6), 2419–2423.

(28) Thommes, M. Physical Adsorption Characterization of Nanoporous Materials. *Chemie Ing. Technol.* **2010**, *82* (7), 1059–1073.

(29) Yuvaraj, S.; Fan-Yuan, L.; Tsong-Huei, C.; Chuin-Tih, Y. Thermal Decomposition of Metal Nitrates in Air and Hydrogen Environments. *J. Phys. Chem. B* **2003**, *107* (4), 1044–1047.

(30) Selinsek, M.; Deschner, B. J.; Doronkin, D. E.; Sheppard, T. L.; Grunwaldt, J.-D.; Dittmeyer, R. Revealing the Structure and Mechanism of Palladium during Direct Synthesis of Hydrogen

https://doi.org/10.1021/acsanm.4c05689
ACS Appl. Nano Mater. XXXX, XXX, XXX–XXX

Peroxide in Continuous Flow Using Operando Spectroscopy. *ACS Catal.* **2018**, *8* (3), 2546−2557.
(31) Grunwaldt, J.-D.; Caravati, M.; Hannemann, S.; Baiker, A. X-Ray Absorption Spectroscopy under Reaction Conditions: Suitability of Different Reaction Cells for Combined Catalyst Characterization and Time-Resolved Studies. *Phys. Chem. Chem. Phys.* **2004**, *6* (11), 3037.
(32) Soni, Y.; Pradhan, S.; Bamnia, M. K.; Yadav, A. K.; Jha, S. N.; Bhattacharyya, D.; Khan, T. S.; Haider, M. A.; Vinod, C. P. Spectroscopic Evidences for the Size Dependent Generation of Pd Species Responsible for the Low Temperature CO Oxidation Activity on Pd-SBA-15 Nanocatalyst. *Appl. Catal. B Environ.* **2020**, *272*, 118934.
(33) Jiao, L.; Regalbuto, J. R. The Synthesis of Highly Dispersed Noble and Base Metals on Silica via Strong Electrostatic Adsorption: II. Mesoporous Silica SBA-15. *J. Catal.* **2008**, *260* (2), 342−350.
(34) Dann, E. K.; Gibson, E. K.; Catlow, C. R. A.; Celorrio, V.; Collier, P.; Eralp, T.; Amboage, M.; Hardacre, C.; Stere, C.; Kroner, A.; Raj, A.; Rogers, S.; Goguet, A.; Wells, P. P. Combined Spatially Resolved Operando Spectroscopy: New Insights into Kinetic Oscillations of CO Oxidation on Pd/γ-Al2O3. *J. Catal.* **2019**, *373*, 201−208.
(35) Reich, J.; Kaiser, S.; Heiz, U.; Grunwaldt, J.-D.; Kappes, M. M.; Esch, F.; Lechner, B. A. J. A Critical View on the Quantification of Model Catalyst Activity. *Top. Catal.* **2024**, *67* (13−14), 880−891.
(36) Al Soubaihi, R. M.; Saoud, K. M.; Myint, M. T. Z.; Göthelid, M. A.; Dutta, J. CO Oxidation Efficiency and Hysteresis Behavior over Mesoporous Pd/SiO_2 Catalyst. *Catalysts* **2021**, *11* (1), 131−148.
(37) Dadi, R. K.; Luss, D.; Balakotaiah, V. Dynamic Hysteresis in Monolith Reactors and Hysteresis Effects during Co-Oxidation of CO and C_2H_6. *Chem. Eng. J.* **2016**, *297*, 325−340.
(38) Hauptmann, W.; Votsmeier, M.; Gieshoff, J.; Drochner, A.; Vogel, H. Inverse Hysteresis during the NO Oxidation on Pt under Lean Conditions. *Appl. Catal. B Environ.* **2009**, *93* (1−2), 22−29.
(39) Etheridge, J. E.; Watling, T. C. Is Reactor Light-off Data Sufficiently Discriminating between Kinetic Parameters to Be Used for Developing Kinetic Models of Automotive Exhaust Aftertreatment Catalysts? The Effect of Hysteresis Induced by Strong Self Inhibition. *Chem. Eng. J.* **2015**, *264*, 376−388.
(40) Amin, A.; Abedi, A.; Hayes, R.; Votsmeier, M.; Epling, W. Methane Oxidation Hysteresis over Pt/Al_2O_3. *Appl. Catal. A Gen.* **2014**, *478*, 91−97.
(41) Abedi, A.; Hayes, R.; Votsmeier, M.; Epling, W. S. Inverse Hysteresis Phenomena During CO and C_3H_6 Oxidation over a Pt/Al_2O_3 Catalyst. *Catal. Lett.* **2012**, *142* (8), 930−935.
(42) Dadi, R. K.; Luss, D.; Balakotaiah, V. Bifurcation Features of Mixtures Containing CO and Hydrocarbons in Diesel Oxidation Catalyst. *Chem. Eng. J.* **2016**, *304*, 941−952.
(43) Casapu, M.; Fischer, A.; Gänzler, A. M.; Popescu, R.; Crone, M.; Gerthsen, D.; Türk, M.; Grunwaldt, J.-D. Origin of the Normal and Inverse Hysteresis Behavior during CO Oxidation over Pt/Al_2O_3. *ACS Catal.* **2017**, *7* (1), 343−355.
(44) Orlik, S. N.; Koval', G. L.; Fesenko, A. V.; Korneichuk, G. P.; Yablonskii, G. S. Kinetics of CO Oxidation on a Palladium-Containing Catalyst. *Theor. Exp. Chem.* **1979**, *15* (1), 59−61.
(45) Al Soubaihi, R. M.; Saoud, K. M.; Ye, F.; Zar Myint, M. T.; Saeed, S.; Dutta, J. Synthesis of Hierarchically Porous Silica Aerogel Supported Palladium Catalyst for Low-Temperature CO Oxidation under Ignition/Extinction Conditions. *Microporous Mesoporous Mater.* **2020**, *292*, 109758−109765.
(46) Maurer, F.; Beck, A.; Jelic, J.; Wang, W.; Mangold, S.; Stehle, M.; Wang, D.; Dolcet, P.; Gänzler, A. M.; Kübel, C.; Studt, F.; Casapu, M.; Grunwaldt, J.-D. Surface Noble Metal Concentration on Ceria as a Key Descriptor for Efficient Catalytic CO Oxidation. *ACS Catal.* **2022**, *12* (4), 2473−2486.
(47) Reich, S.-J.; Svidrytski, A.; Höltzel, A.; Florek, J.; Kleitz, F.; Wang, W.; Kübel, C.; Hlushkou, D.; Tallarek, U. Hindered Diffusion in Ordered Mesoporous Silicas: Insights from Pore-Scale Simulations in Physical Reconstructions of SBA-15 and KIT-6 Silica. *J. Phys. Chem. C* **2018**, *122* (23), 12350−12361.
(48) Gänzler, A. M.; Casapu, M.; Vernoux, P.; Loridant, S.; Cadete Santos Aires, F. J.; Epicier, T.; Betz, B.; Hoyer, R.; Grunwaldt, J. Tuning the Structure of Platinum Particles on Ceria In Situ for Enhancing the Catalytic Performance of Exhaust Gas Catalysts. *Angew. Chemie Int. Ed.* **2017**, *56* (42), 13078−13082.
(49) Zengel, D.; Marchuk, V.; Kurt, M.; Maurer, F.; Salcedo, A.; Michel, C.; Loffreda, D.; Aouine, M.; Loridant, S.; Vernoux, P.; Störmer, H.; Casapu, M.; Grunwaldt, J.-D. Pd Loading Threshold for an Efficient Noble Metal Use in Pd/CeO_2 Methane Oxidation Catalysts. *Appl. Catal. B Environ. Energy* **2024**, *358*, 124363.
(50) Grunwaldt, J.-D.; Wagner, J. B.; Dunin-Borkowski, R. E. Imaging Catalysts at Work: A Hierarchical Approach from the Macro- to the Meso- and Nano-Scale. *ChemCatChem.* **2013**, *5* (1), 62−80.
(51) Bañares, M. A. Operando Methodology: Combination of in Situ Spectroscopy and Simultaneous Activity Measurements under Catalytic Reaction Conditions. *Catal. Today* **2005**, *100* (1−2), 71−77.
(52) Weckhuysen, B. M. Determining the Active Site in a Catalytic Process: Operando Spectroscopy Is More than a Buzzword. *Phys. Chem. Chem. Phys.* **2003**, *5* (20), 4351.
(53) Topsøe, H. Developments in Operando Studies and in Situ Characterization of Heterogeneous Catalysts. *J. Catal.* **2003**, *216* (1−2), 155−164.
(54) Sarma, B. B.; Grunwaldt, J.-D. Operando Spectroscopy to Understand Dynamic Structural Changes of Solid Catalysts. *Chimia (Aarau).* **2024**, *78* (5), 288−296.
(55) Chorkendorff, I.; Niemantsverdriet, J. W. *Concepts of Modern Catalysis and Kinetics*, 3rd ed.; Wiley-VCH: Weinheim, Germany, 2017.
(56) Satsuma, A.; Osaki, K.; Yanagihara, M.; Ohyama, J.; Shimizu, K. Activity Controlling Factors for Low-Temperature Oxidation of CO over Supported Pd Catalysts. *Appl. Catal. B Environ.* **2013**, *132−133*, 511−518.
(57) Busca, G.; Finocchio, E.; Escribano, V. S. Infrared Studies of CO Oxidation by Oxygen and by Water over Pt/Al_2O_3 and Pd/Al_2O_3 Catalysts. *Appl. Catal. B Environ.* **2012**, *113−114*, 172−179.
(58) Onderwaater, W. G.; Taranovskyy, A.; van Baarle, G. C.; Frenken, J. W. M.; Groot, I. M. N. In Situ Optical Reflectance Difference Observations of CO Oxidation over Pd(100). *J. Phys. Chem. C* **2017**, *121* (21), 11407−11415.
(59) Hendriksen, B. L. M.; Bobaru, S. C.; Frenken, J. W. M. Oscillatory CO Oxidation on Pd(100) Studied with in Situ Scanning Tunneling Microscopy. *Surf. Sci.* **2004**, *552* (1−3), 229−242.
(60) Zorn, K.; Giorgio, S.; Halwax, E.; Henry, C. R.; Grönbeck, H.; Rupprechter, G. CO Oxidation on Technological Pd-Al_2O_3 Catalysts: Oxidation State and Activity. *J. Phys. Chem. C* **2011**, *115* (4), 1103−1111.

https://doi.org/10.1021/acsanm.4c05689
ACS Appl. Nano Mater. XXXX, XXX, XXX−XXX